Erschienen in: Advanced Energy Materials ; 4 (2014), 13. - 1400459
https://dx.doi.org/10.1002/aenm.201400459

Darwin at High Temperature: Advancing Solar Cell Material Design Using Defect Kinetics Simulations and Evolutionary Optimization

David P. Fenning, Jasmin Hofstetter, Ashley E. Morishige, Douglas M. Powell, Annika Zuschlag, Giso Hahn, and Tonio Buonassisi**

Material defects govern the performance of a wide range of energy conversion and storage devices, including photovoltaics, thermoelectrics, and batteries. The success of large-scale, cost-effective manufacturing hinges upon rigorous material optimization to mitigate deleterious defects. Material processing simulations have the potential to accelerate novel energy technology development by modeling defect-evolution thermodynamics and kinetics during processing of raw materials into devices. Here, a predictive process optimization framework is presented for rapid material and process development. A solar cell simulation tool that models defect kinetics during processing is coupled with a genetic algorithm to optimize processing conditions in silico. Experimental samples processed according to conditions suggested by the optimization show significant improvements in material performance, indicated by minority carrier lifetime gains, and confirm the simulated directions for process improvement. This material optimization framework demonstrates the potential for process simulation to leverage fundamental defect characterization and high-throughput computing to accelerate the pace of learning in materials processing for energy applications.

1. Introduction

Despite the pressing need to accelerate the development of novel, low-pollution energy technologies, these usually face increased time-to-market because of extensive experimentation required to identify optimal processing conditions. Processing simulation tools may disrupt this status quo by predicting material performance as a function of readily tunable inputs, such as material purity, processing time-temperature profiles, and ambient annealing conditions. However, the application of process simulation tools to energy technologies is lacking in contrast to better developed device simulation tools, which predict device performance given architecture and materials. Improved process simulation tools can bridge the gap between device simulation and manufacturing research and development (R&D), focusing precious resources toward targeted, higher-yield experiments, and accelerating the cycle of learning.

Incorporating these ideas, we present an energy material development paradigm in **Figure 1**, emphasizing the critical interplay of material properties, processing conditions, and device performance while highlighting the opportunity for predictive simulation as a faster route for optimized material processing. To maximize device performance, predictive process and device simulations can be driven by an optimization routine. In this contribution, we show the effectiveness of this approach by coupling a proven silicon solar cell process simulation tool[1] with a genetic algorithm (GA).[2] Process conditions are iteratively optimized to minimize the detrimental impact of metal impurity defects in crystalline silicon-based photovoltaic devices and thereby improve performance. Outputs of the solar cell process simulation include defect distribution and bulk minority carrier lifetime, where the latter serves as important metric for quality control in large-scale manufacturing[3,4] and has been shown by simulations and experiments to be a good predictor of final device performance.[5–9] The resulting guidelines for material improvement indicated by the in silico optimization of processing conditions are confirmed by experiment. While demonstrated with a silicon photovoltaics process model, the framework presented here for predictive optimization of material processing is generalizable for a broad range of energy conversion materials where the goal is to maximize performance over a wide range of input materials.

The behavior of nanoscale defects in bulk silicon have been elucidated by a long history of fundamental experimental and theoretical studies. Metal impurities,[10–17] grain boundaries,[18–20] and dislocations[21,22] have been identified as the principal performance-limiting defects in multicrystalline

Dr. D. P. Fenning,[+] Dr. J. Hofstetter, A. E. Morishige,
D. M. Powell, Prof. T. Buonassisi
77 Massachusetts Avenue, 35–213
Cambridge, MA 02139, USA
E-mail: dfenning@alum.mit.edu; buonassisi@mit.edu
A. Zuschlag, G. Hahn
University of Konstanz
Department of Physics
P. O. Box 676, 78457 Konstanz, Germany
[+]Present address: Department of NanoEngineering, University of California, San Diego, CA 92093

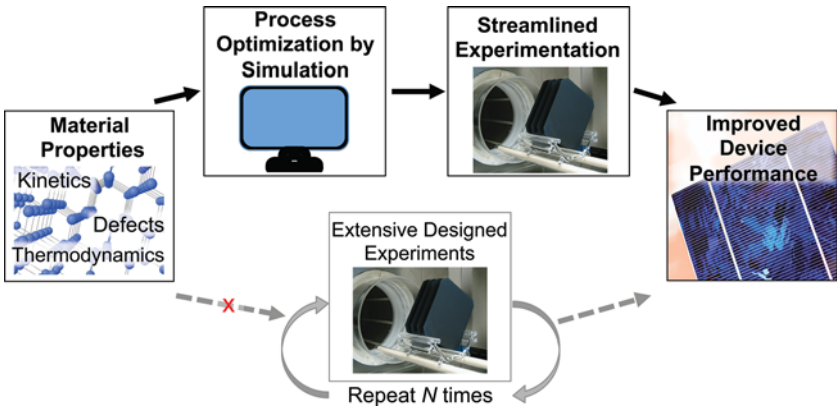

Figure 1. Framework for simulation-guided optimization of processing for renewable energy materials. Leveraging detailed knowledge of material properties and defect behavior from the literature, process simulation can be performed within a genetic algorithm to identify optimum solar-cell processing conditions within user-specified boundary conditions. The result of such process optimization by simulation can be streamlined experimentation and accelerated development.

silicon solar cells and have been investigated extensively both in the as-grown wafer and after solar cell processing. In particular, iron has been the subject of years of detailed microstructural investigations into its point defect[23–26] and overall behavior in silicon,[27–29] which yield insight into both the governing kinetics and thermodynamics during solar-cell processing.[11,30]

We focus on iron here as it remains among the most common and deleterious impurity species affecting the performance of crystalline silicon solar cells.[31–33] The dependence of solar cell performance on iron contamination is complex, as the precise chemical state of iron determines its electronic impact on solar-cell performance. A high concentration of interstitially-dissolved iron (Fe_i) is especially detrimental to bulk electronic performance, whereas second-phase nanoprecipitates of iron-silicide generally have a smaller direct impact.[34,35] Iron can easily transition between dissolved and precipitated states at typical temperatures during solar-cell device fabrication (up to 1000 °C), given the weak binding energy of individual iron atoms to $FeSi_2$ second-phase precipitates.[36–40] The governing reactions, described by coupled non-linear equations with Arrhenius-relationship kinetics, are sufficiently complex to render processing outputs difficult to predict by intuition alone.

2. Simulation of Defect Kinetics during Silicon Solar Cell Processing

The evolution of defects during the processing of a wafer into a solar cell can be described by a set of coupled partial differential equations (PDEs) governing point defect diffusion, segregation to internal or external gettering sites, and precipitate nucleation, growth, or dissolution. Several generations of process simulation tools focused on modeling iron have been developed as the knowledge of structural and electrical defect behavior and interactions[41–44] has increased. The models include the implementations of Ham's law[45–47] or a Fokker-Planck formulation for precipitation,[48,49] simple effective capture cross sections for carrier recombination at precipitates[50,51] or Schottky effect models,[52,53] improved semi-empirical segregation coefficients to gettering layers,[43,54] and models for the growth and chemistry of the gettering layer itself.[55]

Here, we use the Impurity-to-Efficiency (I2E) simulation tool,[47a] which models the essential physics of iron in silicon solar cells in one spatial dimension using Ham's law and maintains a simulation time on the order of 1 min. The I2E simulation tool is freely accessible[47b] and has been experimentally validated.[56–59] Other process optimization tools[46,48,49,60] could potentially be employed in lieu of I2E, provided they have a suitable execution time to allow for reasonable throughput of the optimization routine.

With the help of the I2E tool one can simulate material evolution throughout nearly the entire solar-cell device fabrication process, from junction formation to contact metallization firing.[1,61–63] In this study, we focus on the process step with the largest potential for iron redistribution: phosphorus diffusion gettering, the process step with the largest thermal budget after crystallization. The primary purpose of phosphorus diffusion is forming the n^+-type region of the n^+-p junction, but this phosphorus-rich region simultaneously acts as an external gettering layer for many metal impurities, including iron.[36,38,64,65] The I2E tool simulates external gettering of iron to the phosphorus-rich n^+-type layer, $FeSi_2$ precipitate dissolution and growth, and interstitial iron diffusion.[47]

As inputs to the process simulation, we require the time-temperature profile during the phosphorus diffusion process (variables for later optimization), and the initial iron impurity concentration and distribution, which can be inferred by a combination of analytical techniques.[31,66,67] As outputs, the process simulation computes the final average size of $FeSi_2$ precipitates and the local concentration of Fe_i as a function of depth within the wafer. This bulk defect distribution determines the electronic quality of the silicon wafer, captured by a parameter known as the bulk minority-carrier lifetime (i.e., the electron lifetime in p-type base material considered throughout this work).[32,47,68,69]

From the minority-carrier lifetime distribution, solar-cell device efficiency can be predicted by solving coupled optics and carrier-transport equations. Several simulation packages are commercially or freely available for this purpose,[6] including Sentaurus Device,[8] Silvaco Atlas,[70] SCAPS,[71] PC1D,[5,72] and PC2D.[9] The detailed functional dependence of cell efficiency on minority-carrier lifetime is governed by the specific cell design, but invariably, efficiency increases monotonically (typically, logarithmically) with bulk minority-carrier lifetime.[33] Hence, bulk lifetime can be considered a proxy for cell performance. Consequently, the experimental work presented herein is exclusively focused on the process simulation route to improve bulk minority-carrier lifetime.

3. Applying a Genetic Algorithm (GA) to Material Process Optimization

To identify an optimal solar-cell manufacturing process for a given input material purity, we use the GA to explore phosphorus diffusion processing conditions. As a form of evolutionary optimization, the genetic algorithm begins with a population of "individuals," each consisting of a set of decision variables. The decision variables are the processing conditions we are attempting to optimize. In our case, the decision variables are the temperatures for each time interval in the process, and an individual is the complete time-temperature profile of the phosphorus diffusion process.

The algorithm is initialized with randomly selected temperatures to make up the individuals that form the first generation. For each individual, the algorithm calculates the "evolutionary fitness," the parameter that will be maximized in a single-objective optimization. Here, the fitness is the minority-carrier lifetime resulting from an I2E simulation of the time-temperature profile defining the individual. After the fitness of each individual in the population is calculated, fit individuals, i.e., time-temperature profiles that resulted in high lifetimes, are recombined to form the next generation. Random mutations are injected to promote convergence to global rather than local optima. Over generations, the population of individuals can thus drift toward optimal values (though global optima cannot be guaranteed). The operation of the algorithm is shown schematically in Figure S1 (in Supporting Information). The genetic algorithm employed executes in C++ from the MATLAB command line.[73] Details on the GA parameters used and the I2E simulation can also be found in the Supporting Information.

Given technical and economic limitations typical of high-throughput solar cell manufacture, we examine a phosphorus diffusion parameter space with a temperature range of 700–900 °C and a maximum annealing time of 45 min. We begin with an optimization of hypothetical silicon wafers contaminated with iron at 10 parts per billion atomic (10 ppba, 5×10^{14} cm^{-3}), a concentration regularly found in border areas of cast multicrystalline silicon ingots.[35,74] This relatively high iron concentration leads to poorly performing cells when a standard manufacturing process is applied.[75,76] We assume an initial interstitial iron concentration of 10^{12} cm^{-3}, with the remaining iron uniformly distributed at precipitates 35 nm in radius.[34] Precipitate nucleation during processing is not included in the model. We search for an improved process using the I2E simulation coupled with the GA.

The 45 min high-temperature phosphorus diffusion process is divided into 15 consecutive 3-min intervals, and the temperature of each of those intervals is used as a decision variable in the genetic algorithm. Ten minutes of exponential free-cooling to room temperature is added at the end of each process with a cooling time constant of 6 min. As a first approximation, no constraints were imposed requiring finite ramping times, e.g., the temperature could be 700 °C for one interval followed immediately by 900 °C the next interval. Constant temperatures at each time interval speed the solution of the coupled partial differential equations, as many kinetic properties are strong functions of temperature. Typical simulation time for a single individual was 2 min. An initial population of 60 time–temperature profiles was generated randomly, and the algorithm was stopped after 50 generations. Without parallel processing, the 3000-simulation run takes a total of roughly four days of computational time on a standard PC purchased in 2008 (2× 2.66 GHz Intel Xeon processors, 10 GB RAM).

4. Process Optimization Results

The median and interquartile range of minority-carrier lifetimes resulting from simulation of the population of time-temperature profiles is shown in **Figure 2** for each of the 50 generations for two different initializations of the algorithm. As can be seen, by the end of 50 generations, the median population lifetime is greatly improved, from about 15 µs after the random start to 45 µs, and has stabilized at the same value in both instances, with very little variation in the population around it.

Another visualization of the 3000 simulation results, characteristic of a single run of the genetic algorithm, is achieved by sorting the resulting lifetimes from lowest to highest without regard to which generation they were from, and plotting every 30th time–temperature profile, as shown in **Figure 3**. The lifetime corresponding to each profile is shown in color, with light colors corresponding to poor lifetime, and dark colors corresponding to the best lifetimes.

The best profiles are those that remain at 900 °C before cooling toward the very end of the profile. The plateau temperature is pushed to the limit at 900 °C, maximizing the dissolution of precipitated iron.[77] No benefit is seen to loading at, or ramping up from lower temperatures. Cooling steps toward the end of the profile are important, though, as we see

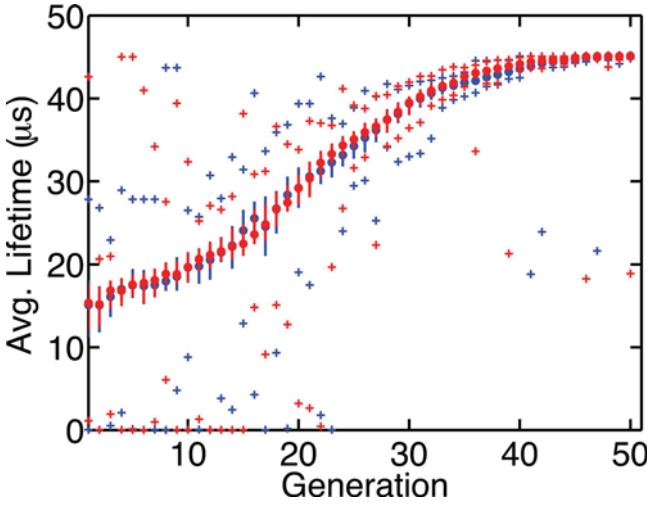

Figure 2. Lifetime distribution over 50 generations of genetic algorithm optimization. The evolution of the median lifetime of the population over the course of the optimization is shown for two instantiations of the genetic algorithm. After random starts that result in a lifetime of 15 µs in both cases, the optimization algorithm converges over 50 generations to the same final lifetime of 45 µs, with little final variation in the population. Circles indicate the median and the bars the interquartile range. Crosses show the minimum and maximum lifetime individual in each generation. Initial total Fe concentration in the wafer was taken to be 10 ppba.

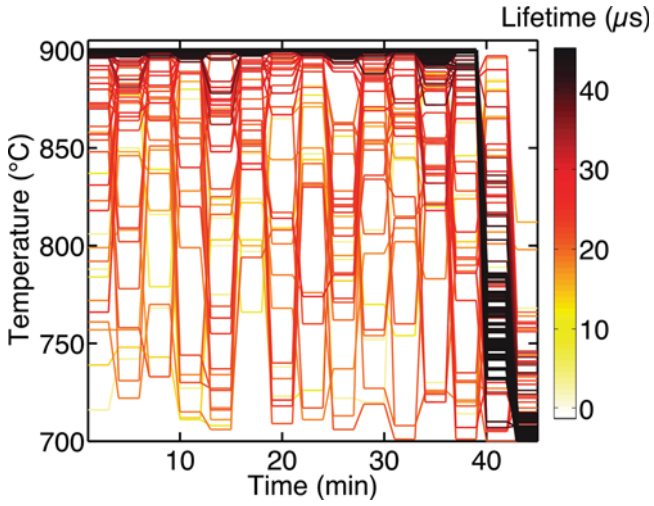

Figure 3. Resulting heat map of the time-temperature parameter space. A heat map of the phosphorus diffusion parameter space indicates the best profiles (dark lines) are those that run at maximum temperature before cooling to the lowest possible temperature at the end of the process. The heat map is produced by sorting the 3000 individual simulations run by the genetic algorithm according to final lifetime and plotting every 30th individual. The genetic algorithm has effectively mapped the entirety of the phosphorus diffusion parameter space.

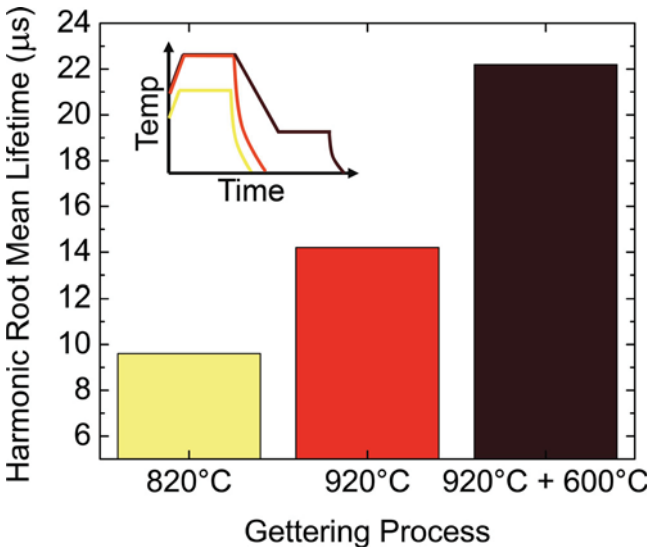

Figure 4. Experimental values of the harmonic root mean lifetime, a strong predictor of cell efficiency, are shown after standard gettering at 820 °C, a higher temperature gettering at 920 °C, and a high-low process at 920 °C + 600 °C. Higher-temperature gettering, particularly when combined with subsequent lower temperature processing, greatly improves performance as predicted by the genetic algorithm optimization. Initial total iron concentration in the wafer was ≈20 ppba.

the algorithm produces the best results when the penultimate interval is around 750 °C and the last step is at 700 °C. This is consistent with experimental findings showing that a slow cool-down or low-temperature anneal after the high-temperature plateau leads to lifetime improvements due to the reduction of interstitial iron.[39,75] Interactions during downstream processes, such as metallization firing, can also affect the iron distribution, due to the thermal profile[62,78] and in part due to hydrogenation,[79] but changes are generally small compared to those during phosphorus diffusion.

After searching widely across the time–temperature parameter space of phosphorus diffusion with 15 degrees of freedom, the unconstrained genetic algorithm optimization suggests a design approach involving the following principles: Moving to high temperature to dissolve and getter precipitated iron, followed by a controlled cooldown to reduce the interstitial iron concentration.

These guidelines were applied in the processing of heavily iron-contaminated multicrystalline samples, containing more than 20 ppba.[77] The spatially resolved minority carrier lifetime after gettering was evaluated for samples from adjacent ingot heights and thus sharing the same crystal defect structure by microwave photoconductive decay with iodine ethanol surface passivation. The resulting harmonic root mean minority carrier lifetime, τ_{av}, a strong predictor of cell efficiency,[80–82] and calculated as $\frac{1}{\sqrt{\tau_{av}}}=\frac{1}{N}\sum_i\frac{1}{\sqrt{\tau_i}}$, from spatially-resolved τ_i, is shown for a typical baseline 820 °C phosphorus diffusion to the left in **Figure 4**. The average lifetime increases significantly after higher-temperature processing at 920 °C. Further significant lifetime improvements are seen when a higher-temperature step at 920 °C is followed by a low-temperature anneal at 600 °C. The higher-temperature gettering step has been shown to dissolve a greater fraction of precipitated iron than the lower-temperature 820 °C step.[77] Adding a low-temperature step drives this dissolved iron to segregate to the emitter, producing significantly better material performance.[39,75] The average lifetime after the higher-temperature steps is now limited by high structural defect density,[83] where phosphorus diffusion is known to be relatively ineffective.[84,85]

To quantify the contributions of the high- and low-temperature components of the diffusion profile to the lifetime improvement seen in the GA process optimization results and the experimental samples, we simulate a sensitivity analysis of the time-temperature process variables. Six variables that define the time-temperature parameter space are chosen for investigation: the temperature at which the samples are loaded into the furnace (Load Temperature), the rate at which they are heated to process temperature (Heating Rate), the temperature of the diffusion step (Plateau Temperature) and its duration (Plateau Time), the cooling rate down from the process temperature (Cooling Rate), and the temperature to which the samples are cooled within the furnace before being unloaded (Unload Temperature). To understand the relative impacts of each of these variables, a one-factor-at-a-time approach is taken where each variable is perturbed around a base case to high and low values. The range of each variable is chosen so that any change in a variable is equivalent to a 15 min deviation in total process time with respect to the base case. In this way, the various time-temperature profile variables can be compared on an equal basis with respect to their impact on throughput. The base case and the high and low values of each variable tested are shown in **Table 1**.

As a fundamental indicator of sensitivity to each process variable, the concentration of Fe_i after gettering is plotted for each case in **Figure 5**, simulated using the same initial iron distribution

Table 1. Parameters in phosphorus diffusion time-temperature profile sensitivity analysis. Each parameter was varied, one at a time, to a high or low value, while the other variables were kept at the base case. Each change in a variable corresponds to a 15 min change in total process time.

Variable	Low Value	Base Case	High Value
Load Temperature [°C]	700	750	800
Heating Rate [°C min^{-1}]	2.2	3.3	7
Plateau Temperature [°C]	820	845	870
Plateau Time [min]	15	30	45
Cooling Rate [°C min^{-1}]	2.2	3.33	7
Unload Temperature [°C]	700	750	800

as that used in the GA. Minority carrier lifetime, which scales inversely with [Fe_i], is shown on the right axis. The base case profile results in a final [Fe_i] just less than 8×10^{10} Fe cm^{-3}. The process variables are arranged from left to right in order of decreasing impact on outcome. Reducing the unload temperature leads to the most significant reduction in interstitial iron to below 4×10^{10} cm^{-3}. Increasing the plateau temperature, increasing the plateau time, and decreasing the cooling rate also lead to modest reductions in final interstitial iron concentration. Conversely, a higher unload temperature significantly increases interstitial iron concentration at the end of the process, more than doubling it. The heating rate and the load temperature have very little impact. The process modifications that lead to the lowest final interstitial iron concentration, low unload temperature and high plateau temperature, agree well with the design principles that result in high lifetime deduced from the genetic algorithm (Figure 3).

To evaluate the results of the sensitivity analysis, the effects of the unload temperature, plateau time, and load temperature (predicted to span a range of sensitivity from large to small)

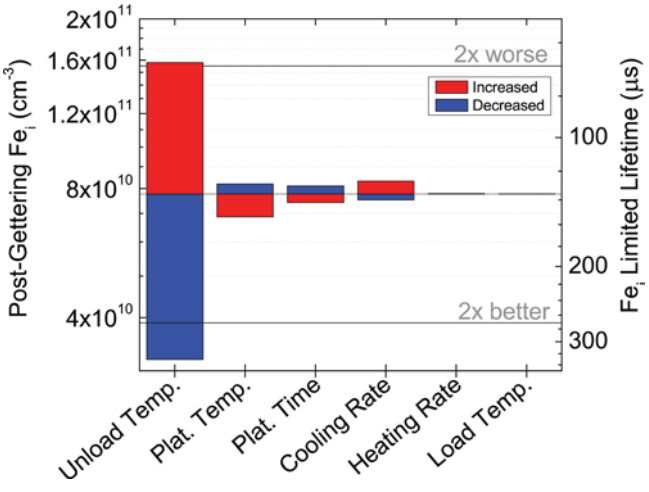

Figure 5. Sensitivity of interstitial iron to process variables. The sensitivity of the post-gettering interstitial iron concentration is plotted for a 15 min deviation in total process time from a base case for six variables. Unload temperature, the temperature to which the samples are cooled before unloading, and the plateau temperature are seen to have the largest potential for reducing final interstitial iron concentration. Initial total iron concentration in the wafer was taken to be 10 ppba.

are tested in an additional experiment on two materials of different contamination level: heavily contaminated multicrystalline silicon (mc-Si) (20 ppba initial [Fe]) and higher purity single-crystal (sc-Si) Czochralski silicon (1 ppba initial [Fe]). The detailed experimental results and simulations thereof are shown in the Supporting Information. All trends of the experiment match the results from I2E process simulation. Absolute values show some discrepancy with the experimental data in a few cases, particularly for slow-cooled low-iron wafers, and are discussed in the SOM and elsewhere.[86] Of the unload temperature, plateau time, and load temperature, the most significant benefits come from slow-cooling and, for the low-iron material, extending the plateau time. The agreement in trends between the experimental and simulated results provides a high degree of confidence in generalizing these results across silicon solar cell materials.

5. Strategies for Overcoming Iron Degradation

To summarize, the high temperature portion of the phosphorus diffusion process is critical to dissolving and removing precipitated iron in low-cost contaminated silicon wafers, leading to the highest lifetimes in the GA and experiments (Figure 3,4). Moving to higher phosphorus diffusion gettering temperatures has been shown to successfully improve lifetimes in heavily-contaminated materials.[77,87–89] An unconstrained optimization of the phosphorus diffusion parameter space by the genetic algorithm pushes the gettering temperature to its allowed maximum. But, a higher gettering temperature alone may not improve results, as it can leave a high interstitial iron concentration if the cooldown from the process temperature happens too quickly. Instead, both simulations and experiments show that employing a slow-cooling step, even for relatively short durations, can dramatically lower the interstitial iron concentration and should be employed when using higher gettering temperatures.

While simulations and experiments presented here focus on highly Fe-contaminated material, design guidelines have been tentatively extracted for low-Fe materials by analogous simulation and experiment (see SOM). Industrial applications can also be constrained by the need to produce a high-performing emitter simultaneously with iron gettering, which requires a sheet resistance in the n-doped surface layer approaching or exceeding 100 Ω/sq.[90] Such constraints can be accommodated in the optimization scheme presented here by applying appropriate penalties to the fitness value for individuals that cause constraint violations.

6. Conclusions

The framework presented herein, whereby a process simulation tool (I2E) is coupled to an evolutionary optimization algorithm, allows one to consider material processing tradeoffs and predict optimal processes, reducing expensive experimental efforts. For the example of silicon solar cells, the time–temperature profile of silicon solar cell processing can significantly alter metal impurity point defect concentrations and precipitate

distributions, and ultimately, dramatically influence the minority-carrier lifetime of the material. By relying on a simple set of equations to describe the most important components of diffusion, segregation, and precipitation of iron during phosphorus diffusion, the I2E process simulation tool allows for large but relatively inexpensive in silico optimization experiments. Using the model in combination with a genetic algorithm, we explore the wide parameter space of phosphorus diffusion to tailor the diffusion process to the starting material quality to extract the full potential from each wafer. The optimization indicates a high-temperature plateau followed by slow-cooling or a low-temperature step reduces the impact of iron impurities.

These design strategies indicated by the genetic algorithm optimization for processing wafers are confirmed by experiments and an additional sensitivity analysis of the time-temperature process parameters. One-factor-at-a-time experiments guided by the simulation experimentally confirm the importance of the plateau temperature and cooling profile on determining the efficacy of iron gettering and final material performance. Observed trends in the simulation and experimental data agree for both single- and multi-crystalline samples with over 20× variation in initial iron concentration.

This methodology focused on predictive optimization of material processing can in principle be extended to other materials systems relevant to emerging renewable energy technologies. In many cases, however, we lack sufficient foundational knowledge of intrinsic and extrinsic point-defect solubility and diffusivity to construct an accurate model. For example, in thin-film quaternary compounds for photovoltaics (e.g., copper zinc tin sulfide), intrinsic point-defect reactions can be complex.[91] Thus, experimental efforts must focus on developing parameterizations of a material's performance-limiting defect kinetics to enable material process optimization by simulation. Then, evolutionary optimization of process conditions using process simulation can drive material and device improvement, potentially more rapidly than a traditional designed experiment strategy focused directly on final performance.

7. Experimental Section

To test the genetic algorithm predictions experimentally, adjacent wafers containing nearly-identical crystal structures were selected from 90% ingot height of an intentionally iron-contaminated boron-doped cast multicrystalline ingot. The wafers contained a resulting total iron concentration of about $\approx 10^{15}$ atoms/cm^3,[76] i.e., an iron content that can be found in the "red zone" border regions of industrial ingots.[35,74]

The as-grown wafers were saw damage etched in acid solution and passivated with iodine ethanol for lifetime characterization. As-grown average lifetimes measured by microwave photoconductive decay (μ-PCD, Semilab WT 2000) were below 1 μs. The iodine ethanol was washed away and several microns etched off to clean the near-surface prior to insertion into the $POCl_3$ diffusion furnace. Single-step diffusions were carried out at 820 °C and 920 °C, resulting in an emitter sheet resistance of 62.6 ± 1.6 and 10.6 ± 0.2 Ω/sq., respectively. The $POCl_3$ deposition for the two-step process was carried out at 920 °C, followed by a cool down of several degrees per min to 600 °C with a 60 min hold at 600 °C (11.5 ± 0.1 Ω/sq.). After phosphorus diffusion, the emitter was etched off and the surfaces repassivated with iodine ethanol for the μ-PCD measurements shown in Figure 4.

Details of the one-factor-at-a-time experiments and results can be found in the Supporting Information.

Supporting Information

Supporting Information is available from the Wiley Online Library or from the author.

Acknowledgements

The authors would like to thank Mariana I. Bertoni and Nathan Stoddard for discussions regarding gettering, and Prof. Jeffrey C. Grossman (MIT) and Prof. Alexander Mitsos (formerly MIT; now RWTH Aachen) for their guidance regarding genetic algorithm optimization. This work was supported by the National Science Foundation (NSF) and the Department of Energy (DOE) under NSF CA No. EEC-1041895. D.P.F. acknowledges the Martin Family Society of Fellows at MIT. J.H. acknowledges Alexander von Humboldt Foundation for support through a Feodor Lynen Fellowship. A.E.M. and D.M.P. acknowledge the Department of Defense through the National Defense Science and Engineering Graduate Fellowship Program. This work was performed in part at the Center for Nanoscale Systems (CNS), a member of the National Nanotechnology Infrastructure Network (NNIN), which is supported by the National Science Foundation under NSF award no. ECS-0335765. Part of this work was financially supported by the German Federal Ministry for the Environment, Nature Conservation and Nuclear Safety and by industry partners within the research cluster "SolarWinS" (contract No. 0325270F).

[1] D. M. Powell, D. P. Fenning, J. Hofstetter, J.-F. Lelièvre, C. Del Cañizo, T. Buonassisi, *Photovoltaics Int.* **2012**, *15*, 91.
[2] D. E. Goldberg, *Optimization and Machine Learning*, Addison-Wesley Longman Publishing Co., Boston, MA **1989**.
[3] J. Haunschild, M. Glatthaar, M. Demant, J. Nievendick, M. Motzko, S. Rein, E. R. Weber, *Sol. Energy Mater. Sol. Cells* **2010**, *94*, 2007.
[4] T. Trupke, K. R. McIntosh, J. W. Weber, W. McMillan, L. Ryves, J. Haunschild, C. Shen, H. Kampwerth, in *Proceedings of the 22nd Workshop on Crystalline Silicon Solar Cells*, Vail, CO, **2012**.
[5] P. Basore, *IEEE Trans. Electron Dev.* **1990**, *37*, 337.
[6] M. Burgelman, J. Verschraegen, S. Degrave, P. Nollet, *Prog. Photovolt: Res. Appl.* **2004**, *12*, 143.
[7] L. Carnel, P. C. Hjems, T. Lu, J. Nyhus, K. Helland, O. Gjerstad, in *Proc. 34th IEEE PVSC*, Philadelphia, PA **2009**, pp. 36–38.
[8] K. Mueller, R. Borges, *Sol. Industry* **2010**, *1*, 1.
[9] P. A. Basore, K. Cabanas-Holmen, *IEEE J. Photovoltaics* **2011**, *1*, 72.
[10] J. R. Davis Jr., A. Rohatgi, R. H. Hopkins, P. D. Blais, P. Rai-Choudhury, J. R. McCormick, H. C. Mollenkopf, *IEEE Trans. Electron Dev.* **1980**, *27*, 677.
[11] E. R. Weber, *Appl. Phys. A* **1983**, *30*, 1.
[12] G. Coletti, P. C. P. Bronsveld, G. Hahn, W. Warta, D. Macdonald, B. Ceccaroli, K. Wambach, N. Le Quang, J. M. Fernandez, *Adv. Funct. Mater.* **2011**, *21*, 879.
[13] M. Heuer, T. Buonassisi, A. A. Istratov, M. D. Pickett, M. A. Marcus, A. M. Minor, E. R. Weber, *J. Appl. Phys.* **2007**, *101*, 123510.
[14] M. Seibt, R. Khalil, V. Kveder, W. Schröter, *Appl. Phys. A* **2009**, *96*, 235.
[15] M. Seibt, D. Abdelbarey, V. Kveder, C. Rudolf, P. Saring, L. Stolze, O. Voß, *Mater. Sci. Eng. B* **2009**.
[16] J. Lindroos, D. P. Fenning, D. J. Backlund, E. Verlage, A. Gorgulla, S. K. Estreicher, H. Savin, T. Buonassisi, *J. Appl. Phys.* **2013**, *113*, 204906.
[17] D. P. Fenning, B. K. Newman, M. I. Bertoni, S. Hudelson, S. Bernardis, M. A. Marcus, S. C. Fakra, T. Buonassisi, *Acta Mater.* **2013**, *61*, 4320.

[18] J. Chen, T. Sekiguchi, D. Yang, F. Yin, K. Kido, S. Tsurekawa, *J. Appl. Phys.* **2004**, *96*, 5490.
[19] K. Kutsukake, N. Usami, T. Ohtaniuchi, K. Fujiwara, K. Nakajima, *J. Appl. Phys.* **2009**, *105*, 044909.
[20] G. Micard, G. Hahn, A. Zuschlag, S. Seren, B. Terheiden, *J. Appl. Phys.* **2010**, *108*, 034516.
[21] B. Sopori, *J. Electron Mater.* **2002**, *31*, 972.
[22] G. Stokkan, S. Riepe, O. Lohne, W. Warta, *J. Appl. Phys.* **2007**, *101*, 053515.
[23] S. Rein, S. W. Glunz, *J. Appl. Phys.* **2005**, *98*, 113711.
[24] A. Liu, Y.-C. Fan, D. Macdonald, *Prog. Photovolt: Res. Appl.* **2011**, *19*, 649.
[25] D. Macdonald, T. Roth, P. N. K. Deenapanray, K. Bothe, P. Pohl, J. Schmidt, *J. Appl. Phys.* **2005**, *98*, 083509.
[26] D. Macdonald, A. Cuevas, J. Wong-Leung, *J. Appl. Phys.* **2001**, *89*, 7932.
[27] A. A. Istratov, H. Hieslmair, E. R. Weber, *Appl. Phys. A* **1999**, *69*, 13.
[28] L. J. Geerligs, Y. Komatsu, I. Roever, K. Wambach, I. Yamaga, T. Saitoh, *J. Appl. Phys.* **2007**, *102*, 093702.
[29] R. Kvande, L. J. Geerligs, G. Coletti, L. Arnberg, M. Di Sabatino, E. J. Øvrelid, C. C. Swanson, *J. Appl. Phys.* **2008**, *104*, 064905.
[30] M. Seibt, A. Sattler, C. Rudolf, O. Voß, V. Kveder, W. Schröter, *Phys. Status Solidi (a)* **2006**, *203*, 696.
[31] D. Macdonald, A. Cuevas, A. Kinomura, Y. Nakano, L. J. Geerligs, *J. Appl. Phys.* **2005**, *97*, 033523.
[32] M. C. Schubert, H. Habenicht, W. Warta, *IEEE J. Photovoltaics* **2011**, *1*, 168.
[33] G. Coletti, *Prog. Photovolt: Res. Appl.* **2013**, *21*, 1163.
[34] T. Buonassisi, A. A. Istratov, M. A. Marcus, B. Lai, Z. Cai, S. M. Heald, E. R. Weber, *Nat. Mater.* **2005**, *4*, 676.
[35] M. C. Schubert, J. Schön, F. Schindler, W. Kwapil, A. Abdollahinia, B. Michl, S. Riepe, C. Schmid, M. Schumann, S. Meyer, W. Warta, *IEEE J. Photovoltaics* **2013**, *3*, 1250.
[36] S. M. Myers, M. Seibt, W. Schröter, *J. Appl. Phys.* **2000**, *88*, 3795.
[37] H. Hieslmair, A. Istratov, S. McHugo, C. Flink, *Appl. Phys. Lett.* **1998**, *72*, 1460.
[38] D. Macdonald, A. Cuevas, F. Ferrazza, *Solid State Electron* **1999**, *43*, 575.
[39] M. D. Pickett, T. Buonassisi, *Appl. Phys. Lett.* **2008**, *92*, 122103.
[40] R. Krain, S. Herlufsen, J. Schmidt, *Appl. Phys. Lett.* **2008**, *93*, 152108.
[41] M. Seibt, H. Hedemann, A. A. Istratov, F. Riedel, A. Sattler, W. Schröter, *Phys. Status Solidi (a)* **1999**, *171*, 301.
[42] W. Schröter, V. Kveder, M. Seibt, A. Sattler, E. Spiecker, *Sol. Energy Mater. Sol. Cells* **2002**, *72*, 299.
[43] A. Haarahiltunen, H. Väinölä, O. Anttila, M. Yli-Koski, J. Sinkkonen, *J. Appl. Phys.* **2007**, *101*, 043507.
[44] P. S. Plekhanov, R. Gafiteanu, U. M. Gösele, T. Y. Tan, *J. Appl. Phys.* **1999**, *86*, 2453.
[45] F. Ham, *J. Phys. Chem. Solids* **1958**, *6*, 335.
[46] H. Hieslmair, S. Balasubramanian, A. A. Istratov, E. R. Weber, *Semicond. Sci. Tech.* **2001**, *16*, 567.
[47] a) J. Hofstetter, D. P. Fenning, M. I. Bertoni, J.-F. Lelièvre, C. del Cañizo, T. Buonassisi, *Prog. Photovolt: Res. Appl.* **2011**, *19*, 487; b) http://pv-i2e.mit.edu, (accessed August 2013).
[48] A. Haarahiltunen, H. Savin, M. Yli-Koski, H. Talvitie, J. Sinkkonen, *J. Appl. Phys.* **2009**, *105*, 023510.
[49] J. Schön, H. Habenicht, M. C. Schubert, W. Warta, *J. Appl. Phys.* **2011**, *109*, 063717.
[50] J. M. Hwang, D. K. Schroder, *J. Appl. Phys.* **1986**, *59*, 2476.
[51] C. del Cañizo, A. Luque, *J. Electrochem. Soc.* **2000**, *147*, 2685.
[52] T. Tan, P. S. Plekhanov, *Mater. Res. Soc. Symp. Proc.* **2001**, *669*, J6.11.1.
[53] P. S. Plekhanov, T. Tan, *Appl. Phys. Lett.* **2000**, *76*, 3777.
[54] H. Talvitie, V. Vähänissi, A. Haarahiltunen, M. Yli-Koski, H. Savin, *J. Appl. Phys.* **2011**, *109*, 093505.
[55] R. Chen, H. Wagner, A. Dastgheib-Shirazi, M. Kessler, Z. Zhu, V. Shutthanandan, P. P. Altermatt, S. T. Dunham, *J. Appl. Phys.* **2012**, *112*, 124912.
[56] J. Hofstetter, D. P. Fenning, J.-F. Lelièvre, C. Del Cañizo, T. Buonassisi, *Phys. Status Solidi (a)* **2012**, *209*, 1861.
[57] J. Hofstetter, J.-F. Lelièvre, D. P. Fenning, M. I. Bertoni, T. Buonassisi, C. del Cañizo, *Solid State Phenom.* **2011**, *178–179*, 158.
[58] D. P. Fenning, J. Hofstetter, M. I. Bertoni, S. Hudelson, M. Rinio, J. F. Lelièvre, B. Lai, C. del Cañizo, T. Buonassisi, *Appl. Phys. Lett.* **2011**, *98*, 162103.
[59] D. P. Fenning, J. Hofstetter, M. I. Bertoni, G. Coletti, B. Lai, C. del Cañizo, T. Buonassisi, *J. Appl. Phys.* **2013**, *113*, 044251.
[60] B. Tryznadlowski, A. Yazdani, R. Chen, S. T. Dunham, in *Proc. 38th IEEE PVSC*, Austin, TX, **2012**, pp. 217–220.
[61] A. E. Morishige, D. P. Fenning, J. Hofstetter, D. M. Powell, T. Buonassisi, in *Proc. 38th IEEE PVSC* **2012**, pp. 002213–002217.
[62] J.-F. Lelièvre, J. Hofstetter, A. Peral, I. Hoces, F. Recart, C. del Cañizo, *Energy Procedia* **2011**, *8*, 257.
[63] A. Peral, J.-F. Lelièvre, F. Recart, C. Del Cañizo, *Phys. Status Solidi (c)* **2012**, *9*, 2107.
[64] M. Sheoran, A. Upadhyaya, A. Rohatgi, *Solid State Electron* **2008**, *52*, 612.
[65] D. Macdonald, A. Cuevas, A. Kinomura, Y. Nakano, in *Proc. 29th IEEE PVSC*, New Orleans, LA, **2002**, pp. 285–288.
[66] T. Buonassisi, M. Heuer, O. Vyvenko, A. Istratov, E. Weber, Z. Cai, B. Lai, T. Ciszek, R. Schindler, *Physica B* **2003**, *340*, 1137.
[67] T. Buonassisi, A. A. Istratov, M. D. Pickett, M. Heuer, J. P. Kalejs, G. Hahn, M. A. Marcus, B. Lai, Z. Cai, S. M. Heald, T. F. Ciszek, R. F. Clark, D. W. Cunningham, A. M. Gabor, R. Jonczyk, S. Narayanan, E. Sauar, E. R. Weber, *Prog. Photovolt: Res. Appl.* **2006**, *14*, 513.
[68] D. Macdonald, A. Cuevas, in *Proc. 16th EU PVSEC*, Glasgow, Scotland, **2000**, pp. 1707–1710.
[69] Y.-C. Fan, J. Tan, S. P. Phang, D. Macdonald, in *Proc. 35th IEEE PVSC*, Honolulu, HI, **2010**, pp. 439–442.
[70] M. Baudrit, C. Algora, I. Rey-Stolle, I. García, B. Galiana, in *Proc. 5th Int. Conf. on Numerical Simulation of Optoelectronic Devices*, IEEE, **2005**, pp. 41–42.
[71] M. Burgelman, P. Nollet, S. Degrave, *Thin Solid Films* **2000**, *361*, 527.
[72] D. Clugston, P. Basore, in *Proc. 26th IEEE PVSC*, Anaheim, CA, **1997**, pp. 207–210.
[73] K. Sastry, *Single and Multiobjective Genetic Algorithm Toolbox for Matlab in C++* **2007**.
[74] T. U. Naerland, L. Arnberg, A. Holt, *Prog. Photovolt: Res. Appl.* **2009**, *17*, 289.
[75] M. Rinio, A. Yodyunyong, S. Keipert-Colberg, Y. P. B. Mouafi, D. Borchert, A. Montesdeoca-Santana, *Prog. Photovolt: Res. Appl.* **2011**, *19*, 165.
[76] S. Riepe, I. E. Reis, W. Kwapil, M. A. Falkenberg, J. Schön, H. Behnken, J. Bauer, D. Kreßner-Kiel, W. Seifert, W. Koch, *Phys. Status Solidi (c)* **2011**, *8*, 733.
[77] D. P. Fenning, A. S. Zuschlag, M. I. Bertoni, B. Lai, G. Hahn, T. Buonassisi, *J. Appl. Phys.* **2013**, *113*, 214504.
[78] B. Michl, J. Schön, F. Schindler, W. Warta, M. C. Schubert, in *Proc. 27th EUPVSEC*, Franfurt, Germany **2012**, pp. 709–713.
[79] P. Karzel, A. Frey, S. Fritz, G. Hahn, *J. Appl. Phys.* **2013**, *113*, 114903.
[80] J. Isenberg, J. Dicker, W. Warta, *J. Appl. Phys.* **2003**, *94*, 4122.
[81] B. Michl, M. Rüdiger, J. A. Giesecke, M. Hermle, W. Warta, M. C. Schubert, *Sol. Energy Mater. Sol. Cells* **2012**, *98*, 441.
[82] H. Wagner, M. Müller, G. Fischer, P. P. Altermatt, *J. Appl. Phys.* **2013**, *114*, 054501.
[83] D. P. Fenning, A. S. Zuschlag, J. Hofstetter, A. Frey, M. I. Bertoni, G. Hahn, T. Buonassisi, *IEEE J. Photovoltaics* **2014**, *4*, 866.

[84] A. Bentzen, B. G. Svensson, E. S. Marstein, A. Holt, *Sol. Energy Mater. Sol. Cells* **2006**, *90*, 3193.
[85] O. Schultz, S. W. Glunz, S. Riepe, G. P. Willeke, in *Proc. EUPVSEC,* Dresden, Germany **2006**, pp. 788–791.
[86] D. P. Fenning, *PhD Thesis*, Massachusetts Institute of Technology, **2013**.
[87] V. Osinniy, A. Nylandsted Larsen, E. Hvidsten Dahl, E. Enebakk, A.-K. Søiland, R. Tronstad, Y. Safir, *Sol. Energy Mater. Sol. Cells* **2012**, *101*, 123.
[88] D. Macdonald, S. P. Phang, F. E. Rougieux, S. Y. Lim, D. Paterson, D. L. Howard, M. D. de Jonge, C. G. Ryan, *Semicond. Sci. Tech.* **2012**, *27*, 125016.
[89] H. J. Möller, C. Funke, M. Rinio, S. Scholz, *Thin Solid Films* **2005**, *487*, 179.
[90] *International Technology Roadmap for Photovoltaic: Results 2012*, SEMI, PV Group, **2013**.
[91] S. Chen, J.-H. Yang, X. G. Gong, A. Walsh, S.-H. Wei, *Phys. Rev. B* **2010**, *81*, 245204.

Darwin at High Temperature: Advancing Solar Cell Material Design Using Defect Kinetics Simulations and Evolutionary Optimization

David P. Fenning, Jasmin Hofstetter, Ashley E. Morishige, Douglas M. Powell, Annika Zuschlag, Giso Hahn, and Tonio Buonassisi

Darwin at High Temperature: Advancing Solar Cell Material Design through Defect Kinetics Simulation and Evolutionary Optimization

David P. Fenning, Jasmin Hofstetter, Ashley E. Morishige, Douglas M. Powell, Annika S. Zuschlag, Giso Hahn, Tonio Buonassisi**

Operation of a genetic algorithm

A schematic of the application of a genetic algorithm to the optimization of energy material processing, in this case the time-temperature profile for iron gettering, is shown in **Figure S1**. After initializing the algorithm with a randomly selected population drawn from the entire parameter space, the fitness of each individual (a set of temperatures that together form the time-temperature profile) is tested with the I2E process simulation.[1] Based on the resulting lifetimes of the population of profiles run, the fittest individuals are selected for recombination and mutation operations that produce the next generation. Each subsequent generation includes elements of the previous generation, evolving toward a maximum.

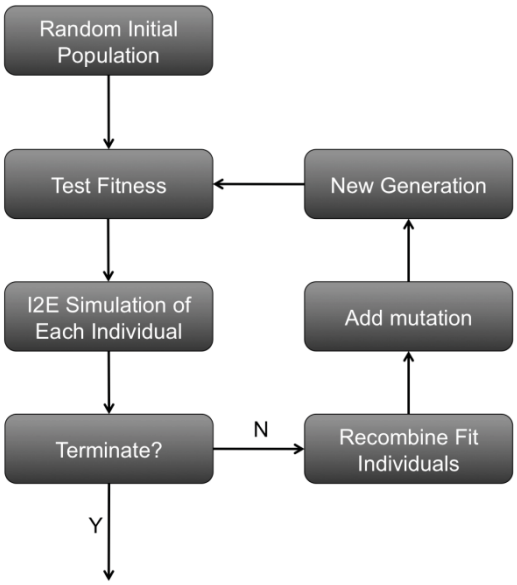

Figure S1. Schematic of the operation of the genetic algorithm.

Parameters of the Genetic Algorithm[2]

An unconstrained, single-objective optimization was performed over a set of fifteen, continuous decision variables – the temperatures corresponding to three-minute segments of a phosphorus diffusion time temperature profile. The domain for each decision variable was the temperature range from 700 to 900°C. The population size at each generation was 60 individuals. The initial population was randomly generated, and each subsequent population was produced by 90% replacement. Each individual's fitness was taken as the minority-carrier lifetime resulting from using the time-temperature profile in an I2E simulation, detailed below. Two rounds of tournament without replacement determined selection. Simulated binary crossover was used for crossover with a swap probability of 50%, and mutation probability was set at 10%. The algorithm was executed for 50 generations.

Impurity-to-Efficiency Simulation Tool

The I2E process simulation tool consists of a system of three partial differential equations describing the kinetics of phosphorus diffusion: interstitial iron diffusion, segregation of interstitial iron to the phosphorus rich regions, and iron precipitate dissolution/growth.[1] The system of equations is numerically solved over time at fixed spatial points. The version of the I2E simulation used in this analysis contains various improvements on previously published work. These include: the enforcement of a minimum iron precipitate radius (2 nm) to prevent instabilities arising from negative precipitate radii, a logarithmically distributed spatial mesh to improve stability, the enforcement of a maximum calculation time step to improve stability, and other numerical modifications.[3] The tool is accessible at http://pv-i2e.mit.edu.

Evolution of Temperature Decision Variables during GA Execution

Figure S2 shows the 15 temperatures that comprise the best individual profile in each of the 50 generations for the instance of the algorithm shown by the blue dots in **Figure 2**. The second instance showed nearly identical results. In **Figure S2**, a line is drawn connecting the value of each decision across generations. As the algorithm begins, there is a high degree of randomness to the best individuals of the first 10 generations as the algorithm covers the 15-dimensional parameter space. Within 20 generations, though, all of the early intervals move toward higher temperatures, while the last two intervals are pushed down to lower temperatures. Generations 40–50 are largely stagnant, with the first 39 min of the profile occurring at the 900°C temperature limit, followed by a step at around 750°C and then a last step at 700°C before the wafers are free-cooled: the best individual in the final generation is shown in the inset and exemplifies this outcome.

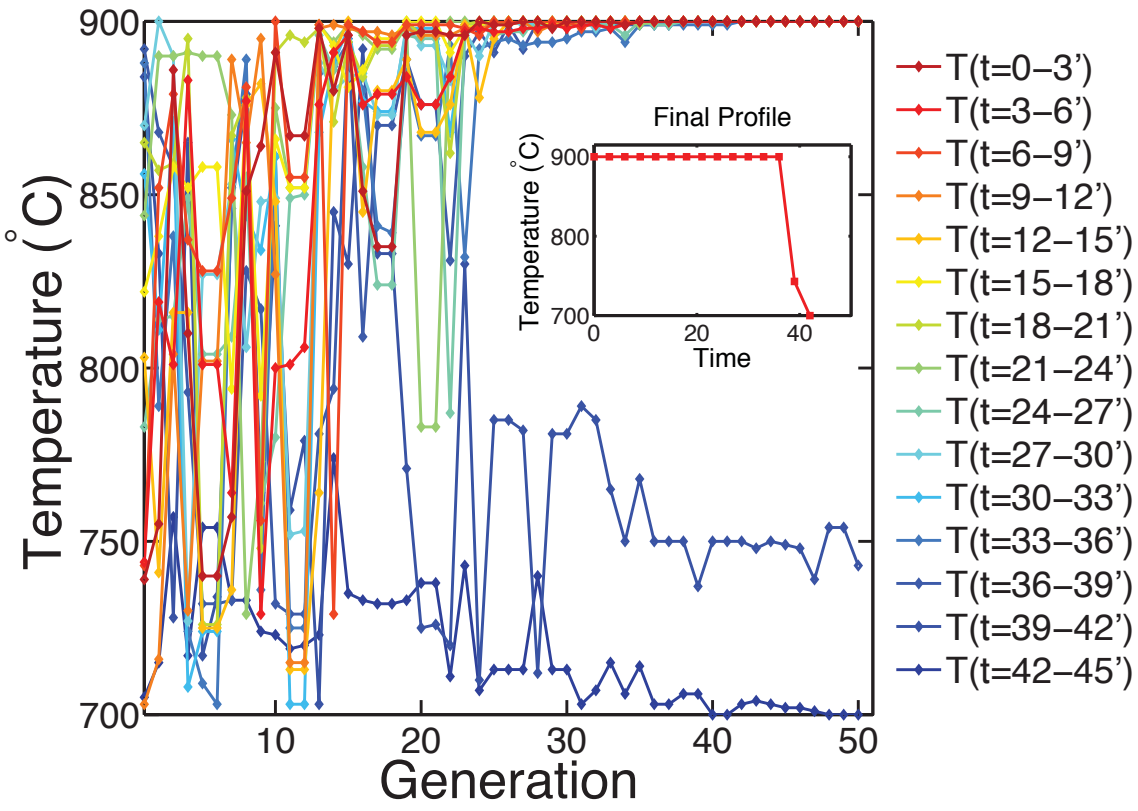

Figure S2. Variation of the Decision Variables during the Optimization. The best individual for each generation is plotted (fifteen points at a single generation), and lines drawn to connect each decision variable of the best individual from generation to generation to track their variation. The temperature variables are listed according to their sequence in the 45 min high-temperature step. During early generations, the best individuals of the population vary widely from generation to generation as the algorithm broadly searches the high-dimensional parameter space. Over time, all of the first 13 temperature intervals converge to the limit at 900°C, while the 14th and 15th steps settle at around 750°C and 700°C respectively. The best time-temperature profile in the 50th generation is shown in the inset.

One-Factor-at-a-Time Experimental Evaluation of Process Variable Sensitivity: Study of Load Temperature, Unload Temperature, and Plateau Time

To evaluate the sensitivity analysis of **Figure 5**, we vary the input material purity for simulation and experimental investigation of the impact of these time-temperature variables using two materials: more heavily contaminated multicrystalline (mc-Si) wafers (20 ppba initial [Fe]) and higher purity single-crystalline material (sc-Si, 1 ppba initial [Fe]). Three variables are varied independently: the *Load Temperature, Unload Temperature,* and *Plateau Time.*

The effect of the *Load Temperature* is explored here as an experimental control, since no change in final interstitial iron concentration is expected from the sensitivity results in **Figure 5**. Extending the high-temperature plateau time should lead to some marginal decrease in the interstitial iron concentration, and the *Unload* process, wherein the wafers are cool to 550°C before removal from the furnace, is expected to show a significant decrease in final interstitial iron concentration. Of the variables analyzed in **Figure 5** that are not investigated below, increasing the *Plateau Temperature* has been shown to lead to improved gettering results in **Figure 3-5** and other studies,[4-6] while the *Cooling Rate* and the *Heating Rate* are constrained experimentally by the tube furnace employed in this study, though their impact is expected to be small.

Materials and Sample Preparation: A set of 175-μm-thick boron-doped adjacent *p*-type mc-Si wafers (0.7 Ω-cm resistivity) from were selected from 90% height of a cast industrial ingot grown from recycled croppings of previous ingots. The recycling of the metal-rich tops of the ingots results in higher contamination levels, approaching the 20 ppba iron noted above, and consequently exhibit lower performance using a standard process. For the sc-Si wafers, a set of standard 290 μm-thick boron-doped *p*-type Czochralski (CZ) wafers (4 Ω-cm resistivity) was used. Sc-Si wafers typically have iron contamination levels at or below commercial mass-spectroscopy detection limits of about 1 ppba.

The as-grown mc-Si wafers were etched in a CP4 acid solution (15 HNO_3:5 CH_3COOH:2 HF) to remove saw damage, followed by a KOH dip to remove re-plated porous silicon left by the CP4 etching. All wafers were then RCA cleaned.[7] Following cleaning, a 20 nm Al_2O_3 surface passivation layer was deposited by atomic layer deposition (ALD) (Cambridge Nanotech), followed by a 400°C anneal for 10 min in N_2 to achieve good surface passivation.[8] Lifetime measurements of float-zone silicon passivated at the same time as the experimental samples achieved lifetimes of over 1 ms, indicating excellent surface passivation quality (<10 cm/s).

Minority-carrier lifetime measurements: Quasi-steady-state photoconductance (QSSPC) measured by a Sinton Instruments WCT-120 was used to take interstitial iron measurements on these as-grown wafers. The measurements were made after exposure to 10 flashes of a Semilab WT-2000 lamp to break Fe-B pairs. Lifetime measurements were then collected after 2–4 hours to allow for repairing. Calculation of interstitial iron concentrations was conducted at an injection condition of 10^{16} cm^{-3}, far away from the crossover point for the Fe-B system.[9]

Phosphorus diffusion: After as-grown lifetime measurements, phosphorus diffusions were conducted in a $POCl_3$ furnace (Tystar Corporation). Four monocrystalline wafers were used for sheet resistance measurements. Four different phosphorus diffusion time-temperature profiles were used:

- *Standard* process: wafers were introduced to the furnace at 800°C, ramped to 845°C for a 25 min plateau with $POCl_3$ deposition, followed by an immediate pull with no cooling within the furnace itself (74.7 ± 1.4 Ω/sq.);

- Low *Load Temperature* process: wafers were loaded into the furnace at 600°C, followed by a ramp to 845°C for a 25 min plateau with $POCl_3$ deposition and immediately pulled, as in the standard process (75.0 ± 1.5 Ω/sq.);
- *Extended* process: matched the *Standard* process except the plateau time was doubled to 50 min (44.7 ± 0.9 Ω/sq.);
- Low *Unload Temperature* process: matched the *Standard* process except that after the 25 min hold at the plateau, the wafers were slowly-cooled at 3–4 °C/min within the furnace until 550°C before unloading (69.1 ± 0.9 Ω/sq.).

These four time-temperature profiles are shown schematically in **Figure S3a**. Four mono- and four multi-crystalline samples were assigned to each diffusion profile to evaluate the iron gettering effect of the process. The ramp rate up to process temperature was 10°C/min in all cases. After phosphorus diffusion, the phosphosilicate glass was stripped off in an HF solution. A CP4 etch was used to remove the emitter, followed by a KOH dip, and an RCA clean. ALD was then used to re-apply an Al_2O_3 passivation layer, as above. Post-diffusion interstitial iron measurements followed the same protocol as the as-grown measurements.

Results

The experimentally measured and simulated average interstitial iron concentrations after gettering are shown for the sc-Si samples in **Figure S3b**. Experimentally, the standard process leads to a final [Fe_i] of approximately 10^{11} cm^{-3}. The process with a lower *Load Temperature* (T_{load} = 600°C, *cf.* **Figure S3a**) resulted in the same final interstitial iron concentration within the error of the experiment, as indicated in the figure by the standard deviation of the four samples at each condition. The process with the extended *Plateau Time* led to a small decrease in interstitial iron. Treating samples with the low *Unload Temperature* process produces a significant decrease in interstitial iron concentration.

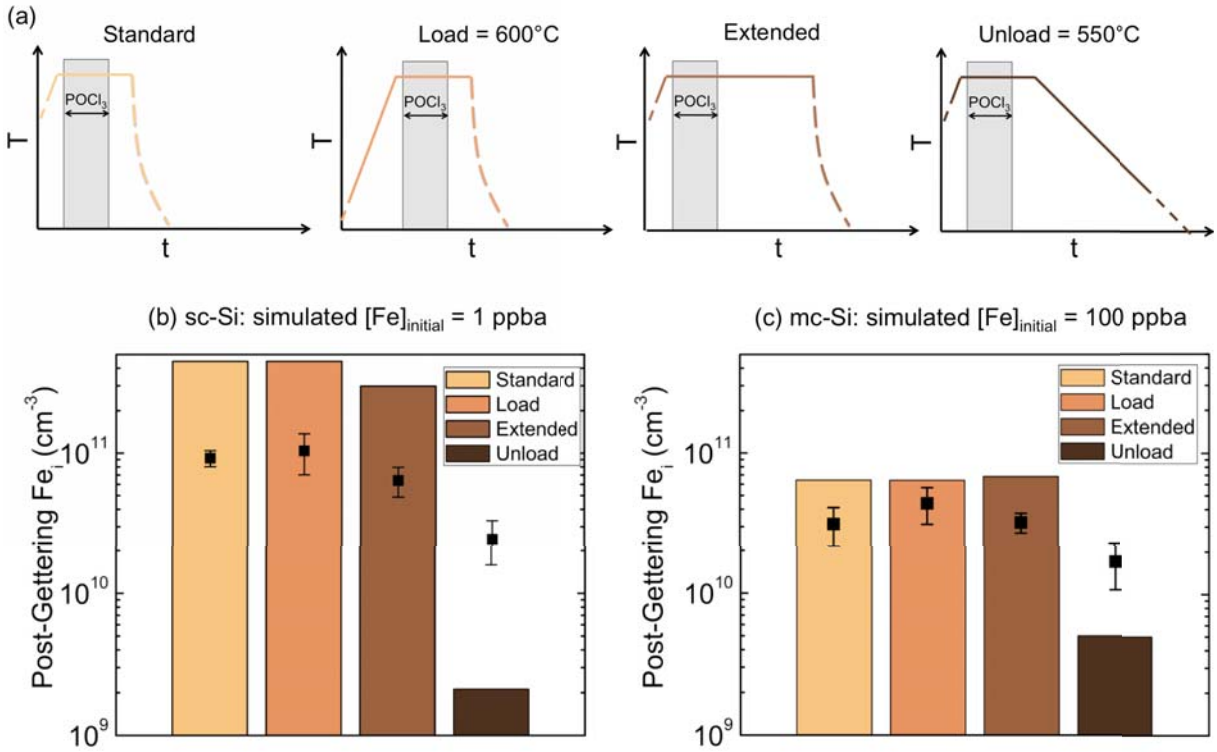

Figure S3. Comparison of Experiment and Simulated Results for Gettering Process Variations. Time-temperature profiles corresponding to each condition are shown in (a). Post-gettering interstitial iron experimentally measured (squares with standard deviation error bars) and simulated (columns) are shown for (b) monocrystalline silicon and (c) multicrystalline silicon.

The experimental results from the mc-Si samples show many of the same trends, as seen in **Figure S3c**. The low *Load Temperature* process does not yield significantly different results than the standard process, as predicted in **Figure 5**. Nor does the extended *Plateau Time* process yield lower interstitial iron, in contrast to the sc-Si results, but revealed by the simulation to be expected due to the high total iron concentration. This is consistent with simulation results shown in **Figure 5** that suggest that for higher total iron concentration, the gettering kinetics are severely limited by precipitated iron in the mc-Si samples[10] and increasing the gettering time has little effect. Instead, higher temperatures have a larger beneficial effect in highly-contaminated samples as seen in **Figures 3-5** and Refs. [4-6] and

indicated in **Figure 5**, relying on the Arrhenius relationship of solubility and diffusivity with temperature to enhance gettering.

The low *Unload Temperature* process still leads to a reduction in interstitial iron concentration after gettering, approaching the detection limit of the measurement at ~10^{10} Fe cm^{-3}. Of note, for the mc-Si samples, the average interstitial iron concentration after gettering was uniformly lower than that for the sc-Si samples for all processes (*e.g.*, the standard process was just over 3×10^{10} Fe cm^{-3} for the mc-Si as compared to nearly 10^{11} Fe cm^{-3} for the sc-Si), most likely as a result of internal gettering to structural defects in mc-Si samples.[11]

Simulations using the same time-temperature profiles corroborate these results and clarify the differences between the response of the low total iron sc-Si wafers and the high total iron mc-Si wafers. A total iron concentration of 1 ppba was assumed for the sc-Si wafers, while 100 ppba was assumed for the mc-Si. Precipitates were assumed to be 22 nm in radius in both materials. **Figure S3b** includes the simulations for the sc-Si wafers. Likewise, **Figure S3c** includes the simulated results for the mc-Si samples.

The lower interstitial iron concentrations for the *Standard*, low *Load Temperature*, and *Extended* processes in the mc-Si samples as compared with the sc-Si samples is reproduced by the simulation. The density of precipitates is much higher in the simulation of the mc-Si sample due to the higher total iron concentration, and internal gettering during the cooldown from process temperature leads to a lower [Fe_i] for mc-Si samples with respect to the sc-Si samples.

While all trends of the experiment agree with the results from I2E process simulation, it is interesting to note that the simulation over-predicts the reduction in interstitial iron during the

unload process in both the mc-Si and sc-Si. There are a number of possible explanations. First, the rate constant used as a fitting parameter to develop the effective segregation coefficient that drives iron gettering has been largely assessed at higher temperatures,[12] though using updated values including low-temperature data[13] does not affect the simulation results significantly. This may be because the solubility of iron below 800°C has been shown by Murphy and Falster[14] to be dependent upon thermal history, perhaps introducing unexpected effects outside of a simple Arrhenius relationship. Second, we model the distribution of precipitates as uniform in size and space, certainly strong assumptions.[5,10,15] Two-dimensional process simulation tools may produce a more accurate assessment of final interstitial iron concentration during cooldown by describing, for example, reprecipitation at heterogeneous structural defects. However, the tradeoff is significantly greater computational expense for 2D simulation. Finally, experimental measurements of samples that were slow-cooled exhibit final interstitial iron concentrations that are often at or below concentrations easily introduced by contamination introduced during wafer "cleaning" in contaminated etchants or during application of surface passivation.[7] While unlikely, such unintentional surface contamination cannot be ruled out at these impurity levels <1 ppta.

Schematic of Process Guidelines

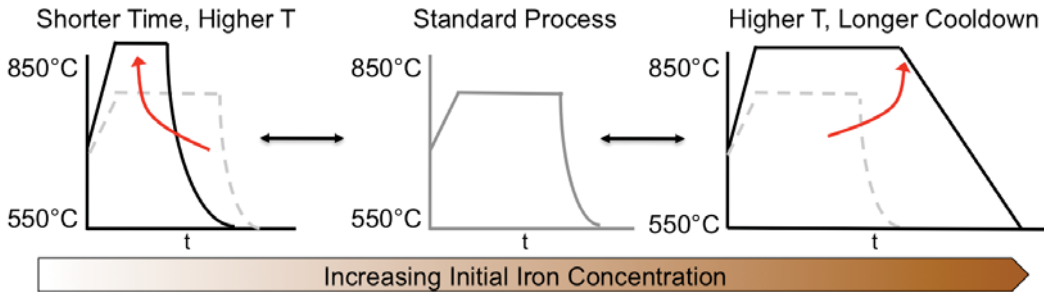

Figure S4. Guidelines for Optimizing Phosphorus Diffusion Gettering.

The general design strategies for improved gettering are shown in **Figure S4**. In iron-limited materials such as border-region multicrystalline silicon, higher gettering temperatures and longer times are required to reduce the precipitated iron concentration and improve bulk lifetime. With a higher gettering temperature must come a controlled cooldown so that the interstitial iron concentration is reduced. In sc-Si materials, less aggressive impurity gettering is generally required.[16,17] A short higher-temperature diffusion may be a way of increasing throughput while achieving the same sheet resistance if lifetimes are adequate for the downstream device structure and efficiency targets. On the other hand, a slow cooldown or low-temperature anneal may be added to drive enhanced segregation gettering, if post-gettered lifetimes need to be improved further and the lifetime-limiting defect after the standard diffusion remains interstitial iron.

REFERENCES:

[1] J. Hofstetter, D. P. Fenning, M. I. Bertoni, J.-F. Lelièvre, C. del Cañizo, T. Buonassisi, *Prog. Photovolt: Res. Appl.* **2011**, *19*, 487.

[2] K. Sastry, *Single and Multiobjective Genetic Algorithm Toolbox for Matlab in C++*; 2007; pp. 1–15.

[3] D. M. Powell, Simulation of Iron Impurity Gettering in Crystalline Silicon Solar Cells, Massachusetts Institute of Technology.

[4] V. Osinniy, A. Nylandsted Larsen, E. Hvidsten Dahl, E. Enebakk, A.-K. Søiland, R. Tronstad, Y. Safir, *Solar Energy Materials and Solar Cells* **2012**, *101*, 123.

[5] D. Macdonald, S. P. Phang, F. E. Rougieux, S. Y. Lim, D. Paterson, D. L. Howard, M. D. de Jonge, C. G. Ryan, *Semicond Sci Tech* **2012**, *27*, 125016.

[6] D. P. Fenning, A. S. Zuschlag, M. I. Bertoni, B. Lai, G. Hahn, T. Buonassisi, *Journal of Applied Physics* **2013**, *113*, 214504.

[7] A. A. Istratov, H. Hieslmair, E. R. Weber, *Appl Phys A-Mater* **2000**, *70*, 489.

[8] B. Hoex, S. B. S. Heil, E. Langereis, M. C. M. van de Sanden, W. M. M. Kessels, *Appl. Phys. Lett.* **2006**, *89*, 042112.

[9] D. Macdonald, T. Roth, P. N. K. Deenapanray, T. Trupke, R. A. Bardos, *Appl. Phys. Lett.* **2006**, *89*, 142107.

[10] D. P. Fenning, J. Hofstetter, M. I. Bertoni, G. Coletti, B. Lai, C. del Cañizo, T. Buonassisi, *Journal of Applied Physics* **2013**, *113*, 044251.

[11] A. Liu, D. Walter, S. P. Phang, D. Macdonald, *IEEE Journal of Photovoltaics* **2012**, *2*, 479.
[12] A. Haarahiltunen, H. Savin, M. Yli-Koski, H. Talvitie, J. Sinkkonen, *Journal of Applied Physics* **2009**, *105*, 023510.
[13] H. Talvitie, V. Vähänissi, A. Haarahiltunen, M. Yli-Koski, H. Savin, *Journal of Applied Physics* **2011**, *109*, 093505.
[14] J. D. Murphy, R. J. Falster, *Journal of Applied Physics* **2012**, *112*, 113506.
[15] T. Buonassisi, A. A. Istratov, M. D. Pickett, M. Heuer, J. P. Kalejs, G. Hahn, M. A. Marcus, B. Lai, Z. Cai, S. M. Heald, T. F. Ciszek, R. F. Clark, D. W. Cunningham, A. M. Gabor, R. Jonczyk, S. Narayanan, E. Sauar, E. R. Weber, *Prog. Photovolt: Res. Appl.* **2006**, *14*, 513.
[16] A. Laades, K. Lauer, M. Blech, C. Maier, D. Alber, M. Baehr, A. Lawerenz, Hamburg, Germany, 2009; p. 2157.
[17] T. M. Pletzer, S. Suckow, E. F. R. Stegemann, H. Windgassen, D. L. Bätzner, H. Kurz, *Prog. Photovolt: Res. Appl.* **2012**, *21*, 900.